



CrossMark
click for updates

Cite this: *RSC Adv.*, 2015, 5, 78508

Stable room temperature magnetic ordering and excellent catalytic activity of mechanically activated high surface area nanosized $\text{Ni}_{0.45}\text{Zn}_{0.55}\text{Fe}_2\text{O}_4$ †

S. Dey,^a R. Gomes,^b R. Mondal,^a S. K. Dey,^a P. Dasgupta,^c A. Poddar,^c V. R. Reddy,^d A. Bhaumik^{*b} and S. Kumar^{*a}

Herein we report the structural, microstructural, dc magnetic and hyperfine properties along with catalytic activity of mechanosynthesized nanosized $\text{Ni}_{0.45}\text{Zn}_{0.55}\text{Fe}_2\text{O}_4$ (~12 nm). The Rietveld refinement of the powder X-ray diffraction data, high resolution transmission electron microscopy and the infield Mössbauer study suggest that the sample is nanosized pure single phase cubic spinel of $Fd\bar{3}m$ symmetry with good crystallinity and it possesses equilibrium cation distribution ($(\text{Fe}^{3+}_{0.45}\text{Zn}^{2+}_{0.55})_A[\text{Fe}^{3+}_{1.55}\text{Ni}^{2+}_{0.45}]_B\text{O}_4$). The sample exhibits ferrimagnetic ordering with high saturation magnetization ($M_{\text{SAT}} = 53, 72$ and 76 emu g^{-1} at 300, 100 and 10 K, respectively), coercivity ($H_C = 280, 1200$ and 2800 Oe at 300, 100 and 10 K, respectively), collective magnetic excitations, spin canting and memory effect in dc magnetization. The infield Mössbauer study suggests that the interior region of the particles is perfectly ferrimagnetic in nature, while the spins at the surface region are ferrimagnetically coupled but noncollinearly aligned. Despite its nanometric size, the sample does not show superparamagnetic behavior but rather retains stable magnetic order at room temperature due to enhancement of stress and surface anisotropy energy caused by high energy ball milling. We have shown that the presence of collective magnetic state along with surface spin disorder are the underlying reason for having slow dynamics and memory effect in the sample. Further, the BET (Brunauer–Emmett–Teller) surface area and the pore volume of the sample are $233 \text{ m}^2 \text{ g}^{-1}$ and $0.475 \text{ cm}^3 \text{ g}^{-1}$, respectively. The temperature programmed desorption (TPD) of ammonia suggests that the surface of this porous material is highly acidic ($1.516 \text{ mmol g}^{-1}$). Because of its high surface acidity and BET surface area the material acts as an efficient heterogeneous catalyst in the one pot synthesis of 3,4-dihydropyrimidine-2(1*H*)-ones (DHPMs) by Biginelli condensation reaction. This sample can be used in magnetic data storage devices, coding, storing and retrieving of binary numbers through magnetic field change and also as a very efficient heterogeneous, magnetically separable and recyclable catalyst.

Received 25th July 2015

Accepted 7th September 2015

DOI: 10.1039/c5ra14773e

www.rsc.org/advances

Introduction

Among all the currently studied magnetic nanomaterials, nanometric ferrites are the most popular ones not only for technological reasons but also due to their importance in understanding the fundamentals of nanomagnetism.^{1–9} The unique physical properties of nanometric ferrites have been the focus of extensive research in recent years. The nanometric

ferrites exhibit interesting structural properties and rich crystal chemistry.⁹ They are also regarded as an exemplary model system for understanding the underlying mechanism of superparamagnetism, spin glass like behavior, spin canting effect and ferrimagnetism.⁹ The interest in the study on magnetic properties of nanostructured ferrites is fueled by their applications in high density data storage devices, magnetic resonance imaging (as contrast agent), magnetically guided drug delivery, hyperthermia treatment.^{9–15} However, with decreasing particle size the magnetic anisotropy energy liable to clutch the magnetization along certain orientation becomes comparable to the thermal energy and due to this the magnetic moment flips randomly with time. When this happens, particles lose their magnetic order and become superparamagnetic.^{9,16} The stability of magnetic order can be accomplished by the enhancement of the anisotropy energy.⁹ In

^aDepartment of Physics, Jadavpur University, Kolkata-700 032, India. E-mail: kumars@phys.jdvu.ac.in

^bDepartment of Materials Science, Indian Association for the Cultivation of Science, Kolkata-700 032, India. E-mail: msab@iacs.res.in

^cSaha Institute of Nuclear Physics, 1/AF Bidhannagar, Kolkata-700064, India

^dUGC-DAE CSR, University Campus, Khandwa Road, Indore-452001, India

† Electronic supplementary information (ESI) available. See DOI: 10.1039/c5ra14773e

recent times, the mechanically activated ferrites have come out as the potential candidates in the perspective of overcoming the direct clash between need for miniaturization and inherent superparamagnetic character of magnetic nanoparticles.^{3,9}

It is noteworthy that the stress anisotropy induced by ball milling acts as an extra source of anisotropy energy and it helps in retaining the stable magnetic order of the nanosized Ni–Zn ferrite at room temperature.⁹ A lot of investigations have been performed on nanometric $\text{Ni}_x\text{Zn}_{1-x}\text{Fe}_2\text{O}_4$ ferrites because of their high saturation magnetization, chemical stability and bio degradability.^{3,9,16–21} The Néel temperature (T_N) of mechanically milled $\text{Ni}_{0.5}\text{Zn}_{0.5}\text{Fe}_2\text{O}_4$ increases significantly ($T_N \sim 592$ K) compared to its bulk counterpart ($T_N \sim 538$ K) due to cation redistribution.¹⁷ The strengthening of intersublattice J_{AB} interaction promoted by the migration of Fe^{3+} ions from (A) to [B] site leads to the enhancement of magnetization ($M_{\text{SAT}} \sim 51.3$ and 113.4 emu g^{-1} at 300 and 10 K, respectively), coercivity ($H_C \sim 500$ and 1000 Oe at 300 and 10 K, respectively) and anisotropy energy of the mechanically milled nanosized (~ 25 nm) $\text{Ni}_{0.35}\text{Zn}_{0.65}\text{Fe}_2\text{O}_4$.³ The cation redistribution, chemical inhomogeneity and large microstrain result in enhancement of magnetic order, magnetic ordering temperature ($T_B \sim 240$ K), saturation magnetization ($M_{\text{SAT}} \sim 42$ and 64 emu g^{-1} at 300 and 10 K, respectively) and coercivity ($H_C \sim 1000$ Oe at 10 K) along with subsequent reduction of superparamagnetic relaxation in mechanically alloyed $\text{Ni}_{0.35}\text{Zn}_{0.65}\text{Fe}_2\text{O}_4$ (~ 27 nm).²¹ Reduction of magnetization and magnetic ordering temperature of nanosized ferrites caused by surface spin canting and superparamagnetic relaxation are well established phenomena but despite some attempts the origin of counterintuitive enhancement of magnetization and magnetic ordering temperature in mechanically activated nanometric ferrites is yet not been understood properly.

Beside the issues related with magnetism, the ferrite nanoparticles have enormous potential for wide variety of catalytic applications.^{22–29} Recently, the nanosized ferrites have emerged as easily recyclable and recoverable catalysts for various organic reactions by discarding the hazardous process of separation and recycling of catalyst using conventional methods.²² This has immense importance in the field of green chemistry. For example, the nanometric CuFe_2O_4 acts as a competent reusable initiator in the synthesis of β,γ -unsaturated ketones from different allyl halides and acid chlorides,²⁸ the catalyst–oxidant combination of NiFe_2O_4 and H_2O_2 has been used in the oxidation of thiols to disulfides and sulfides to sulfoxides,²⁹ ZnFe_2O_4 nano powders have been successfully utilized as a catalyst for the one pot three component synthesis of 4*H*-pyrans in water¹⁴ while the Ni–Co ferrite nanoparticles are efficient candidate for the reduction of nitro aromatic compounds and photo-oxidative degradation of toxic dyes.²⁷

It has been reported that the mechanically activated nanosized Ni–Zn ferrites are magnetically superior compared to its counterparts synthesized by chemical routes.^{3,9,16,21} As most of the applications rely on the stability of magnetic order of the nanoparticles with time and high magnetization at room temperature therefore the mechanically activated nanosized Ni–Zn ferrites of different compositions deserve much more

attention. To the best of our knowledge, there is no report on the structural, magnetic, hyperfine properties and catalytic activity of mechanically activated nanosized $\text{Ni}_{0.45}\text{Zn}_{0.55}\text{Fe}_2\text{O}_4$. In this background, we have synthesized the nanosized $\text{Ni}_{0.45}\text{Zn}_{0.55}\text{Fe}_2\text{O}_4$ by high energy ball milling, rigorously characterized it by using powder X-ray diffraction (PXRD), transmission electron microscopy (TEM), scanning electron microscopy (SEM), energy dispersive X-ray spectroscopy (EDS), and Mössbauer spectroscopic techniques and thoroughly examined the magnetic and hyperfine properties of the sample in order to reveal the role of microstrain, cation redistribution and stress anisotropy induced by ball milling in determining the magnetic and hyperfine properties of the sample. Moreover, we have evaluated the catalytic activity of the sample through the synthesis of 3,4-dihydropyridin-2-1*H*-(ones) (DHPMs) by solvent-free one-pot Biginelli condensation reaction.

In this context, it is pertinent to mention that the functionalized 3,4-dihydropyrimidine-2(1*H*)-ones (DHPMs) can be used for a variety of biological and pharmacological activities which include antibacterial, antifungal and antihypertensive as well as anticarcinogenic applications. They can act as α/a -adrenogenic antagonists, neuropeptide mitotic kinesine inhibitors and HIV gp-120-CD₄ inhibitors.^{30,31} The synthetic route of such DHPMs follows a one-pot multi-component condensation reaction (Biginelli condensation) between an aldehyde, a β -keto ester and urea. The reaction can be catalyzed by various Lewis and Brønsted acids as well as bases. The drawbacks associated with homogeneous catalysts are catalyst separation, product isolation, low yield and stringent reaction condition. So an easily removable solid acid catalyst giving high yield of products is desirable.^{32,33} Herein we have studied the role of mechanically activated nanosized $\text{Ni}_{0.45}\text{Zn}_{0.55}\text{Fe}_2\text{O}_4$ as a magnetically removable catalyst for the synthesis of DHPMs for the first time.

Experimental section

Materials

We have used powder oxides of $\alpha\text{-Fe}_2\text{O}_3$, NiO and ZnO. All the oxides are of 99.99% purity and have been procured from Sigma Aldrich.

Synthesis

Bulk $\text{Ni}_{0.45}\text{Zn}_{0.55}\text{Fe}_2\text{O}_4$ has been prepared by standard ceramic method. At first all the oxides were mixed together in stoichiometric ratio and then manually grounded in an agate mortar for few hours. After that, the mixture was pelletized at a pressure of 20 tons cm^{-2} . The pellets were sintered at 900 °C for 12 h and cooled down to room temperature at a rate of 3 °C min^{-1} . The pellets were grounded again and then passed through the same process of sintering at temperature 950 °C. Finally, the sample was annealed at 700 °C for 12 h and slowly cooled down to the room temperature.

The nanosized $\text{Ni}_{0.45}\text{Zn}_{0.55}\text{Fe}_2\text{O}_4$ was synthesized by grinding course powders of extremely pure $\text{Ni}_{0.45}\text{Zn}_{0.55}\text{Fe}_2\text{O}_4$ prepared by standard ceramic method at ambient temperature using Fritsch Planetary Mono Mill Pulverisette 6. The speed of the grinder was

set at 330 rpm. Grinding was carried out for 50 hours with ball to mass ratio of 20 : 1 using Tungsten Carbide vials and balls.

Experimental

The PXRD pattern of the sample was recorded by Bruker D8 Advanced Diffractometer using Cu K α ($\lambda = 1.54184 \text{ \AA}$) radiation by setting the generator at 40 kV and 40 mA. The data was collected at room temperature (21 °C) over the range of $2\theta = 15\text{--}80^\circ$ with step size and counting time of 0.0199° and 5 s per step, respectively. The high resolution transmission electron (HRTEM) micrographs of the sample were recorded by JEOL 2100 HRTEM. The FESEM (FEI, INSPECT F50) was used for the morphological and microstructural characterizations. The presence of constituent elements in the sample was probed by BRUKER EDS system attached with the FESEM equipment. The Fourier transform infrared (FTIR) spectrum of the sample was recorded by Perkin Elmer spectrometer (Spectrum Two) equipped with attenuated total reflectance (ATR) attachment in the wave number range of $400\text{--}4000 \text{ cm}^{-1}$.

The dc magnetization (M) as a function of temperature (T) and external magnetic field (H) was measured using superconducting quantum interference device magnetometer (Quantm Design, SVSM, USA). The Mössbauer spectra of the sample were recorded in transmission geometry using constant acceleration drive (CMTE-250) with a 25 mCi ^{57}Co source. The Mössbauer spectrum of the sample at 10 K in an external magnetic field of 5 T applied parallel to the γ -ray direction was recorded using superconducting magnet (JANIS Super-OptiMag). The natural iron sample is used as standard. The Mössbauer spectra of the sample were fitted by Recoil program.³⁴ In all the spectra the solid lines indicate the simulated curves and the solid circles represent experimental data points.

The N_2 adsorption/desorption isotherm of the sample was recorded in a Quantachrome Instrument Autosorb 1C at 77 K. The sample was degassed at 453 K for 3 h under high vacuum before the analysis. Non local density functional theory was employed for the determination of the pore size distribution from the N_2 adsorption/desorption isotherm. The temperature programmed desorption (TPD) profile of ammonia over nano-sized $\text{Ni}_{0.45}\text{Zn}_{0.55}\text{Fe}_2\text{O}_4$ nanomaterial has been analyzed by using a thermal conductivity detector (TCD) in a Micromeritics Chemisorb 2720 instrument. For this experiment, the sample (372 mg) was first degassed in flow of He (flow rate 30 cm^3) for 2 hours at 100 °C. Then the sample was saturated with 10% NH_3 in He at room temperature for 30 minutes. The excess NH_3 was removed by flow of He (flow rate 30 cm^3) for 45 minutes and after that the temperature programmed desorption of ammonia (carrier gas He) was studied by heating the sample from room temperature to 700 °C at a temperature ramp of $10 \text{ }^\circ\text{C min}^{-1}$.

The catalytic reactions were carried out in an Anton Paar microwave reactor Monowave 300. In a typical reaction β -keto ester (8 mmol), aldehyde (8 mmol), urea (12 mmol) and our sample as catalyst (30 mg) were mixed thoroughly and irradiated in the reactor for 10 minutes at 120 °C under solvent-free condition. After completion of the reaction

mixture was cooled to room temperature and 10 ml ethanol was added to it and the catalyst was removed magnetically. The mixture was evaporated to dryness and the resultant solid product was stirred in water and filtered. The product was washed with hexane and recrystallized from hot ethanol to obtain in pure form. The products were characterized by ^1H and ^{13}C NMR and compared with reported values. This procedure was followed to prepare all the dihydropyrimidinones.

Result and discussion

Structural studies

It is well known that the cation redistribution is a common feature of nanosized ferrites.⁹ So, to determine the crystal structure of nanosized ferrite unambiguously the information about the cation migration is required.⁹ Therefore, we have recorded the infield Mössbauer spectrum of the sample at 10 K in the presence of 5 T external magnetic field. The infield Mössbauer spectrum exhibits two clear subpatterns (Fig. 1(a)). The non-zero intensity of the 2nd and 5th line in the infield Mössbauer pattern indicates the presence of spin canting,^{21,35} which is mainly regarded as a surface phenomena.^{9,21} Moreover, many uncommon magnetic features of ferrite nanoparticles have been explained by core-shell model, where it is assumed that the spins in the interior region (core) of the particle are perfectly aligned while the spins at the surface (shell) region are noncollinear in nature.^{16,21} To account for the effect of diverse structural and magnetic character of the surface and core of the sample together we have fitted the infield spectrum with two pairs of sextets by assuming that the sample is composed of ferrimagnetically aligned core (interior region) surrounded by magnetically disordered shell (surface region). Further, to verify the validity of this assumption, the without field Mössbauer spectrum at 10 K has been fitted by four Lorentzian sextets

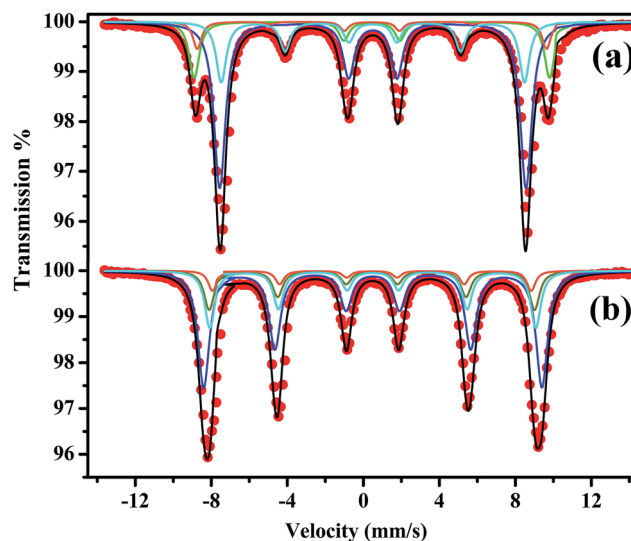


Fig. 1 Mössbauer spectra of the sample at (a) 10 K with 5 T external magnetic field and (b) 10 K fitted by the "Lorentzian site analysis" of the Recoil program.

maintaining the relative occupancies of the Fe^{3+} ions among the (A) and [B] sites same as those obtained from fitting of the infield pattern. The simulated and the experimentally observed patterns are presented in Fig. 1 and the values of hyperfine parameters are listed in Table 1. Following the standard practice, the pair of sextet with high canting angle and low hyperfine field (HMF) is assigned to the shell region of the particles, whereas the pair with high HMF and very small canting is ascribed to the ferrimagnetically ordered core.^{3,9} In each pair the sextet with higher hyperfine field (HMF) and lower isomeric shift (IS) accounts for the (A) site Fe^{3+} ions, while the other sextet with lower HMF and higher IS takes care of the [B] site Fe^{3+} ions.^{3,9} The resultant curves obtained by simulation matches well with the experimentally observed Mössbauer patterns (Fig. 1) and the values of hyperfine parameters obtained by fitting the infield and without field Mössbauer spectra are in good agreement with each other (Table 1). From the calculated values of the canting angles (Table 1) it may be inferred that the spins at the surface region of the particle is highly disordered, while the core behaves like almost perfect ferrimagnetically ordered systems. This endorses the fact that the basic assumption adopted for the fitting of infield Mössbauer spectrum at 10 K is correct and further confirms that the particles of the sample are composed of ferrimagnetically ordered core surrounded by a ferrimagnetic shell with disordered spin structure. The results of infield and without field Mössbauer studies together with suggest that only Fe^{3+} ions are present in the sample.³ The ratio of $\text{Fe}^{3+}_A/\text{Fe}^{3+}_B$ has been calculated from the relative area of the sextets.³ The values of $\text{Fe}^{3+}_A/\text{Fe}^{3+}_B$ at core region and at the surface are 0.291 and 0.298, respectively. These are nearly equal. The average value of $\text{Fe}^{3+}_A/\text{Fe}^{3+}_B$ is 0.2945 and it is used during structural refinement for providing the initial occupancies of Fe^{3+} ions at (A) and [B] site.⁹

The indexing of the PXRD pattern, initial structural and microstructural characterization together with phase analysis were carried out by using NTREOR90 of EXPO2009 package, DICVOL06 and TREOR90 of Fullprof.2k package, FINDSPACE of EXPO2009 package and Rietveld based software package MAUD2.33.^{36–40} The details of the methodology adopted for structural, microstructural and phase analysis was reported by

Table 2 Crystal data and refinement parameters obtained by MAUD^a and GSAS^b programs

Parameters	Values
Formula ^{a,b}	$\text{Ni}_{0.45}\text{Zn}_{0.55}\text{Fe}_2\text{O}_4$
Formula weight ^{a,b}	238.06
Crystal system ^{a,b}	Cubic
Space group ^{a,b}	$Fd\bar{3}m$
Crystallite size (nm) ^a	11.70(0.06)
Microstrain ($\times 10^{-4}$) ^a	2.393(0.4)
a^b (Å)	8.4150(6)
V^b [Å ³]	595.885(2)
Z^b	8
$D_{\text{cal}}^b/\text{g cm}^{-3}$	5.307
$\mu_{\text{CuK}\alpha}^b/\text{mm}^{-1}$	84.334
R_{wp}^a	0.020
R_{exp}^a	0.014
GOF ^a	1.43
R_{wp}^b	0.0118
R_p^b	0.0105
R_f^{2b}	0.1935
χ^2^b	1.727

our group earlier.^{9,21,41,42} The Rietveld refinement plot obtained by using MAUD2.33 is presented in Fig. S1.† The refinement converges with negligible difference between the experimental and simulated data and satisfactory values of reliability parameters. The relevant structural, microstructural and reliability parameters are listed in Table 2.

To determine the crystal structure, bond length and bond angle of the sample more precisely we performed the Rietveld refinement of the PXRD data using GSAS program⁴³ with EXPGUI interface (Fig. 2).⁴⁴ The occupancies of the iron ions at the (A) and [B] sites were provided according to the value of the ratio of $\text{Fe}^{3+}_A/\text{Fe}^{3+}_B$ (0.2945) as obtained from the infield Mössbauer study as initial input. The details of the methodology followed here is available in our earlier reports.⁹ The results suggest that the sample is a single phase spinel ferrite and it has crystallized in space group $Fd\bar{3}m$ of f.c.c. lattice with structural formula $(\text{Zn}^{2+}_{0.55}\text{Fe}^{3+}_{0.45})_A[\text{Ni}^{2+}_{0.45}\text{Fe}^{3+}_{1.55}]_B\text{O}_4$. It is noteworthy that the cation distribution in the sample is almost equal to the ideal equilibrium value of bulk $\text{Ni}_{0.45}\text{Zn}_{0.55}\text{Fe}_2\text{O}_4$.

Table 1 Values of zero field and infield Mössbauer parameters of the sample at 10 K determined by Lorentzian profile analysis of Recoil program

Temperature/field	Site	Width (mm s^{-1})	IS (mm s^{-1})	2ϵ (mm s^{-1})	B_{eff}^a (T)	B_{hf} (T)	A_{23}	θ^b (degree)	Area (%)
10 K/5 T	$[\text{Fe}^{3+}_A]_s$	(±0.03) 0.25	(±0.03) 0.45	(±0.03) 0.00	(±0.4) 57.0	(±0.4) 52.3 ^c	(±0.02) 0.250	20.06	(±0.2) 6.9
	$[\text{Fe}^{3+}_B]_s$	0.30	0.50	0.01	49.5	53.0 ^c	1.450	46.80	23.1
	$[\text{Fe}^{3+}_A]_c$	0.30	0.45	0.00	58.0	53.0 ^c	0.002	1.80	15.8
	$[\text{Fe}^{3+}_B]_c$	0.35	0.50	0.02	50.0	55.0 ^c	0.010	4.05	54.2
10 K/0 T	$[\text{Fe}^{3+}_A]_s$	0.25	0.45	0.00	—	52.0	—	—	6.9
	$[\text{Fe}^{3+}_B]_s$	0.30	0.50	0.01	—	53.2	—	—	23.1
	$[\text{Fe}^{3+}_A]_c$	0.30	0.45	0.00	—	53.1	—	—	15.8
	$[\text{Fe}^{3+}_B]_c$	0.35	0.50	0.02	—	55.4	—	—	54.2

^a Observed HMF (BHF) is the vector sum of the internal HMF and the external applied magnetic field. ^b The average canting angle estimated from the ratio of the intensities of lines 2 and 3 from each subspectra, I_2/I_3 (A_{23}) according to $\theta = \arccos[(4 - I_2/I_3)/(4 + I_2/I_3)]^{1/2}$. Where $I_2/I_3 = A_{23}$. ^c Estimated according to the relationship of B_{eff} , B_{hf} and applied field.

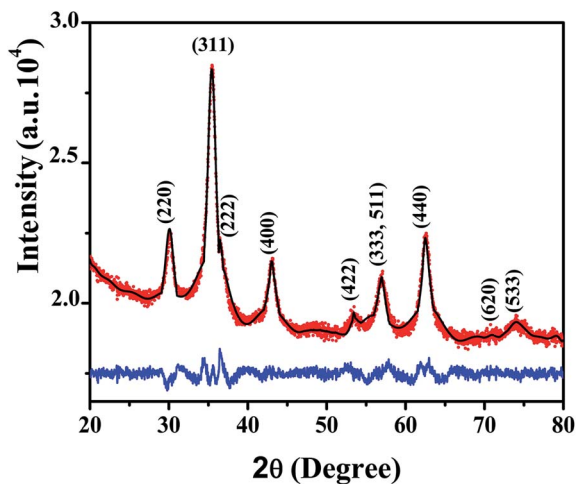


Fig. 2 The Rietveld refinement plot of the sample using GSAS, showing the difference (blue color line) between the experimental (red color symbol) and the simulated pattern (black color line).

The Miller indices and the space group obtained by the Rietveld structure refinement method are in good agreement with JCPDS database (JCPDS no. 08-0234). Fig. 3 depicts the asymmetric unit, surroundings of metal and oxygen ions, bond angle and bond length and the values of structural and microstructural parameters and fractional coordinates along with the occupancy of different ions are listed in Tables 2 and 3.

HRTEM, FESEM and FTIR study

The transmission electron microscopy and selected area electron diffraction (SAED) technique were employed for comprehensive structural and microstructural (particle size, shape and crystallinity) characterization of the sample. The TEM micrographs at low and high magnification along with SAED pattern are shown in Fig. 4. The individual size of the particles in the sample is in the range of 8–20 nm, the particles in the sample are of assorted size and irregular shape (Fig. 4(a)–(c)). The particle size distribution histogram is fitted with a log-normal function and the fitting suggests that the average particle size is ~ 12 nm, which corroborates the crystallite size obtained from

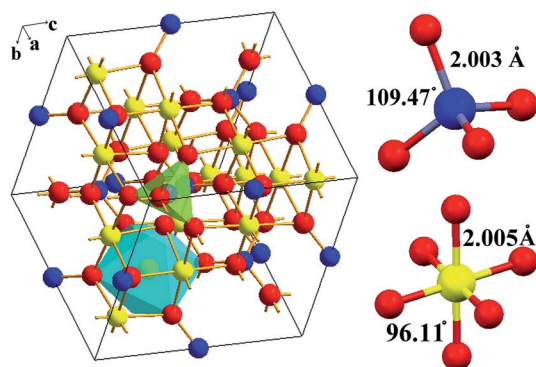


Fig. 3 Unit cell of the sample showing the tetrahedral (A) and octahedral (B) sites, along with the bond angles and lengths.

Table 3 Fractional coordinates and occupancy of different ions obtained by GSAS program

Ions	x	y	z	Occupancy (± 0.002)
Zn(A)	1/8	1/8	1/8	0.550
Fe(A)	1/8	1/8	1/8	0.450
Fe(B)	1/2	1/2	1/2	0.775
Ni(B)	1/2	1/2	1/2	0.225
O	0.2624(12)	0.2624(12)	0.2624(12)	1.000

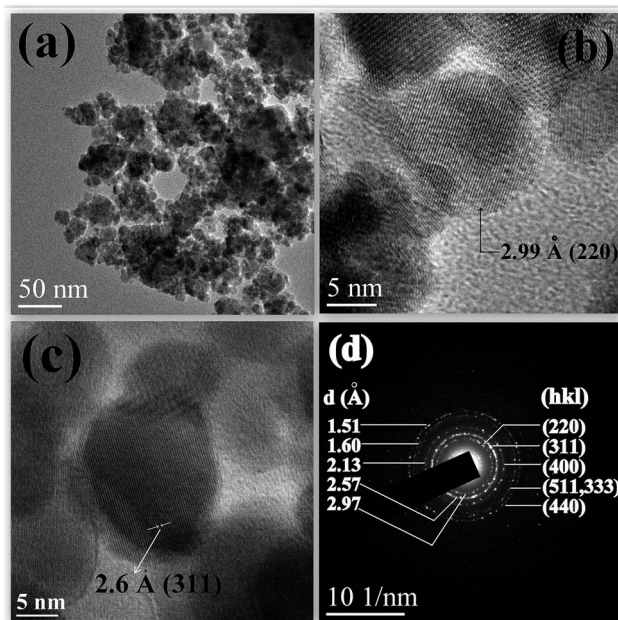


Fig. 4 (a), (b) and (c) HRTEM micrograph and (d) SAED pattern of the sample.

the PXRD study. The good polycrystalline nature of the sample is confirmed by the gleaming lattice fringes in the HRTEM image (Fig. 4(c)) and prominent Debye–Scherrer rings in the SAED pattern (Fig. 4(d)).¹⁶ The crystallographic “*d*” values calculated from the radius of the rings corresponding to the different lattice spacing are in consonance with the values obtained from the PXRD study.

The energy dispersive X-ray spectrum of the sample has been shown in Fig. S2.† The well-resolved peaks originating from the constituent atoms have been found in the energy range from 0 to 8 keV. The peak attributed to Au $L\alpha$ appears as the sample was coated with gold prior to EDS study. In addition, elemental mapping (Fig. S3†) also indicates the presence of all the constituent elements (Fe, Ni, Zn and O). The FTIR spectrum of the sample is shown in Fig. S4.† The absorption bands at about 427 and 538 cm^{-1} are attributed to the stretching vibrations of the octahedral and tetrahedral site metal–oxygen bonds, respectively.⁴⁵ Thus the FTIR study supports the results of PXRD study.

N₂ adsorption/desorption analysis

The N₂ adsorption/desorption isotherm for the sample is shown in Fig. 5. This isotherm has the characteristic features of both

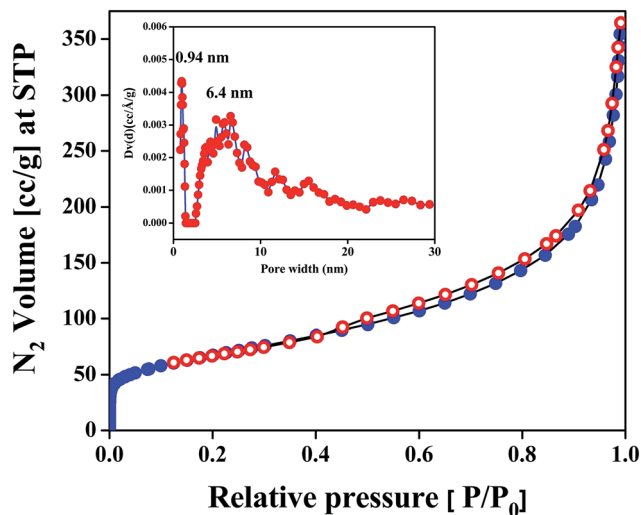


Fig. 5 N_2 adsorption/desorption isotherms of the sample at 77 K. Adsorption points are marked by filled circles and desorption points by empty circles. Pore size distributions obtained by using NLDFT method is shown in the inset.

type I (at low P/P_0 region) and type IV (at high P/P_0 region) isotherms. Further, this isotherm also shows a mild hysteresis loop in the pressure region 0.5–0.9 P/P_0 of N_2 , indicating the presence of large mesopores.⁴⁶ The BET (Brunauer–Emmett–Teller) surface area and a pore volume of the porous sample are $233 \text{ m}^2 \text{ g}^{-1}$ and $0.475 \text{ cm}^3 \text{ g}^{-1}$, respectively. The nonlocal density functional theory (NLDFT) is used to determine the pore size distribution of the sample (inset of Fig. 6), where two types of pores: micropore with pore width of 0.94 nm and mesopore of 6.4 nm are observed. The interparticle porosity of *ca.* 6.4 nm could be attributed to the observed mild hysteresis.

Magnetic nanoparticles have an inherent tendency to form agglomerates. It may be noted that we have adopted a special

technique for TEM sample preparation to prevent the inherent tendency of agglomerate formation.¹⁶ In spite of that agglomerates are observed in the HRTEM image (Fig. 4) due to very high magnetization of the sample. The HRTEM images (Fig. 4) give no evidences in favor of the presence of intragranular pores in the sample. It may therefore be inferred that the intergranular pores have been formed in between the boundaries of the particles. The HRTEM study suggests that the particles in the sample are of irregular shape and assorted size. The variation in pore size can be attributed to the irregular shape and assorted size of the particles.

TPD profile of ammonia

The NH_3 -TPD profile of the porous sample is presented in Fig. 6 which shows two peaks at temperatures 348 and 558 K. The low temperature peak represents weak acidic site and is comparatively smaller than the other one. It corresponds to a surface acidity of $0.416 \text{ mmol g}^{-1}$. Whereas, the high temperature peak indicates the presence of strong acidic sites corresponding to 1.1 mmol g^{-1} . Thus the total acidity of the material is $1.516 \text{ mmol g}^{-1}$. The Lewis acidity of the transition metals present at the surface of this porous material could be responsible for such high surface acidity.

Magnetic and hyperfine property

The ZFC–FC magnetization curves of the sample at an external magnetic field of 500 Oe are shown in Fig. 7. The ZFC magnetization remains almost independent of temperature between 300 and 120 K (T_f) and tumbles rapidly on further cooling. The FC magnetization increases leisurely on cooling and gets almost saturated below 10 K. The nature of the ZFC–FC curves is far and away different from those obtained in purely superparamagnetic system.⁹ No signature of superparamagnetic blocking has been observed up to 300 K. Similar type of behavior in ZFC–FC magnetization curves has been earlier

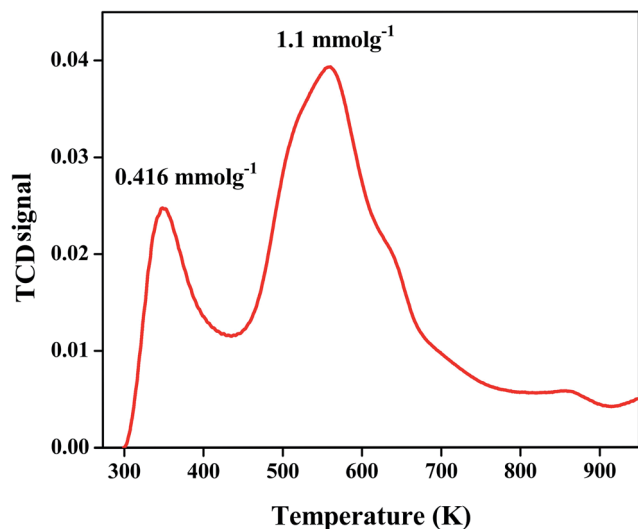


Fig. 6 Temperature programmed desorption profile of NH_3 of the sample.

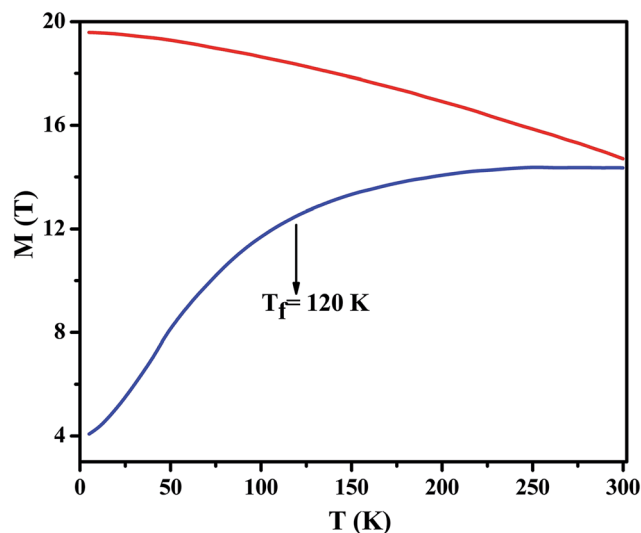


Fig. 7 ZFC–FC magnetization of the sample at 500 Oe external magnetic field.

observed for mechano-synthesized $\text{Ni}_{0.5}\text{Zn}_{0.5}\text{Fe}_2\text{O}_4$,⁹ $\text{Co}_{0.2}\text{Zn}_{0.8}\text{Fe}_2\text{O}_4$ ^{47,48} and ZnFe_2O_4 ⁴⁹ nanoparticle systems and explained in the paradigm of collective magnetic state and spin glass like behavior.

The sample exhibits clear hysteresis loop at room temperature ($H_C = 280$ Oe), which indicates that the sample is in magnetically well ordered state at this temperature (Fig. 8). The high value of coercive field has been observed in the $M-H$ curves (inset of Fig. 8) recorded at lower temperatures ($H_C = 1200$ and 2800 Oe at 100 and 10 K, respectively). The saturation magnetization (M_{SAT}) of the sample has been calculated from the M vs. $1/H$ plot using the law of approach to saturation. The values of M_{SAT} at 300, 100 and 10 K are 53, 72 and 76 emu g^{-1} , respectively. Moreover, the nonsaturated nature of the magnetization curve up to 5 T external magnetic field may be ascribed to the presence of spin canting in the sample.²¹

It is well known that the magnetic ordering of the iron containing materials can be easily investigated with the help of ⁵⁷Fe Mössbauer spectroscopic technique.^{3,9,16,21,50-55} The Mössbauer spectrum at 300 K (Fig. 9) has been fitted by Lorentzian site analysis method of the Recoil program. The Mössbauer spectrum at 300 K consists of a relaxed sextet (76.2%) and a superparamagnetic doublet (23.8%), which suggest that the blocking temperature (T_B) of the system is higher than room temperature, most of the particles (72.2%) in the sample exhibit the phenomenon of collective magnetic excitation and the rest are in superparamagnetic state.²¹ The magnetization vector of the particles in collective magnetic state fluctuates very slowly but remains close to easy axis while the magnetization vector of particles in superparamagnetic state flip randomly with faster rate.³ Moreover, it is well known that for system exhibiting superparamagnetic relaxation and collective magnetic excitation, the outcome of an experiment depends upon the window time of the measurement technique adopted.³ Due to the lower window time of Mössbauer spectroscopy ($\sim 10^{-7}$ to 10^{-9} s) compared to dc magnetic measurement (~ 100 s), it succeeded in probing the presence of superparamagnetic state in the sample, the signature of which has not been found in the dc magnetization measurements.¹⁶ It may be noted that the room temperature Mössbauer spectrum has been recorded without applied magnetic field while the ZFC

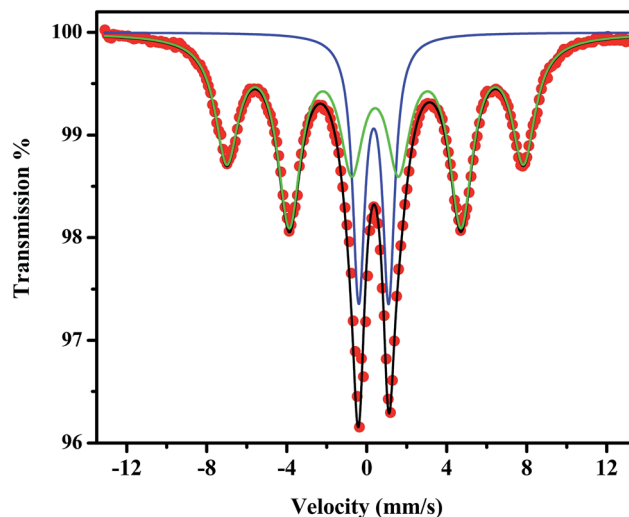


Fig. 9 Mössbauer spectrum of the sample at 300 K fitted by the "Lorentzian site analysis" of the Recoil program.

magnetization has been recorded in presence of 500 Oe field. The results of ZFC-FC magnetization together with the Mössbauer spectroscopic study suggests that 500 Oe field is enough to align the magnetization vectors of the particles in collective magnetic state.³ As most of the particles in the sample are in collective magnetic state (72.2%) and dc magnetic measurement provides the information regarding the magnetic character of a sample as a whole, so the contribution coming from few superparamagnetic particles has been masked in the ZFC-FC magnetizations and $M-H$ measurement. Because of this, the ZFC magnetization remains constant in the temperature range 120–300 K and the $M-H$ loop at room temperature has displayed hysteresis.⁹

The abrupt and rapid fall of ZFC magnetization below 120 K reveals that the magnetic moments of the particles in the sample get frozen randomly below this temperature.⁹ Under such a situation, the local magnetic order persists and Mössbauer spectroscopy, being a sensitive local tool for probing hyperfine character, can easily provide the information about such local magnetic order.^{3,9} In fact the Mössbauer spectrum at 10 K exhibits a clear sextet and gives evidence in favor of the existence of local magnetic order in the sample (Fig. 1(b)).⁹ This result suggests that the thermal fluctuation induced relaxation has been completely wiped out in low temperature and the system is either in magnetically ordered state as a whole or there are certain regions in the sample which are magnetically ordered.³ The abrupt fall of ZFC magnetization below 120 K discards the possibility of existence of magnetically well ordered state below this temperature. The low temperature $M-H$ and Mössbauer spectroscopic studies indicate the presence of spin canting. Thus by keeping in mind the outcomes of dc magnetic and Mössbauer study at low temperature, it may be inferred that the sharp drop of the magnetic moment below T_f in the ZFC magnetization curve is caused by the random freezing of the canted surface spins and the cooperative freezing of magnetic moments exhibiting collective magnetic excitation. In collective

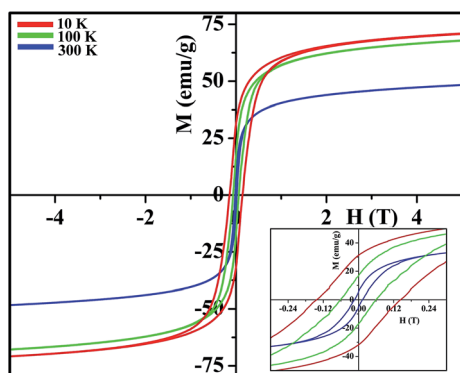


Fig. 8 $M-H$ (hysteresis) loops of the sample at 300, 100 and 10 K. (inset shows the $M-H$ loops between ± 0.3 T for clarity).

state, the particles in the system behave like an assembly rather than an individual one and the anisotropy energy of such an assembly shows multimimima in phase space.³ This type of system can display spin glass like freezing behavior below a certain temperature (T_f) due to cooperative freezing of the magnetic moments.⁹ Therefore we propose that the magnetic moment of the sample drops sharply below 120 K (T_f) as the core region of the particles in the sample undergoes magnetic phase transition from collective magnetic state to spin glass like state through cooperative freezing of spins at the core region and the random freezing of the spins at the surface due to spin canting effect. Further, it is true that in spin glass like state the magnetization falls rapidly but the coercive field remains unaffected and due to this the sample displays hysteresis below 120 K.³

Now a days, the industrial applications of ferrite nanoparticles demand stable magnetic order and high magnetization at room temperature.⁹ However, in most of the cases the unstable spontaneous magnetization at higher temperature in consequence of superparamagnetism and reduction of magnetization caused by spin canting severely limit their application possibilities. The dc magnetic study together with infield and without field Mössbauer spectroscopic study reveal that the sample under investigation is magnetically well ordered at 300 K along with it displays substantial amount of coercive field ($H_C = 280$ Oe) and this has been noticed only in very few nanometric ferrites.^{3,9} It may be noted that the high energy ball milling has induced large microstrain among the lattice planes, ample amount of grain boundary defect together with shape and size irregularity which collectively enhance the stress and surface anisotropy of the system.⁹ Thus the total anisotropy energy of the system gets enhanced. The extra anisotropy contribution due to high energy ball milling has positive contribution in maintaining stable magnetic order at room temperature and promoting high coercivity.⁹

Moreover, the M_{SAT} at 300 K (53 emu g^{-1}) has been found to be the highest among all the reported values of M_{SAT} s of mechanochemically synthesized Ni–Zn ferrite nanoparticles at the same temperature.⁹ It is well known that the magnetization of nanometric ferrites depends upon the relative distribution of magnetic cations between tetrahedral [A] and octahedral [B] sites of spinel lattice and the canting angle between [B] site moments. In most of the nanometric ferrites magnetization reduces due to unfavorable migration of magnetic cations between [B] to [A] site and surface spin disorder or both.^{3,47,48} In our earlier work on nanosized $\text{Ni}_{0.5}\text{Zn}_{0.5}\text{Fe}_2\text{O}_4$, we have proposed that the inherent tendency of the reduction of magnetization of nanometric ferrites due to surface spin canting can be countered by maintaining equilibrium cation distribution.⁹ Even though the present sample exhibits high surface spin canting, it maintains the equilibrium cation distribution which helps in retaining high magnetization in the sample.

Magnetic coding experiment

We have performed the memory experiment (Fig. 10) on the sample by adopting the following steps: (i) at first, an external

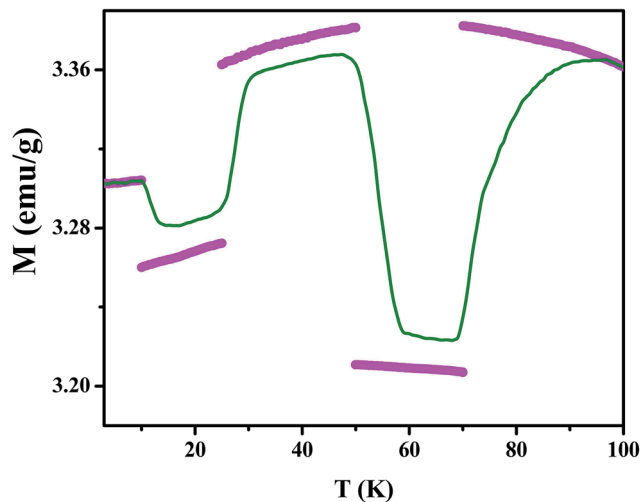


Fig. 10 Memory effect in the dc magnetization of the sample (green line indicates heating cycle and the solid pink circles represent the cooling cycle).

magnetic field of 100 Oe was switched on and the sample was cooled down below 300 K and the magnetization was recorded, (ii) after reaching at 70 K, the 100 Oe field was switched off and the system was detained in the same state for 1 h and then the 100 Oe field was restored and the sample was cooled down to 50 K, (iii) at 50 K, the field was switched on to 200 Oe and the system was arrested at this state for 1 h and then 100 Oe field was restored and the system was cooled down to 25 K, (iv) at 25 K, the 100 Oe field was switched off and the system was maintained in that state for 1 h, after that the 100 Oe field was restored and the system was cooled down to 10 K, (v) at 10 K, 200 Oe field was switched on and the system was arrested at this state for 1 h, then the 100 Oe field was restored and the system was cooled down to 3 K and (vi) finally the system was heated back from 3 K in the presence of 100 Oe magnetic field and the magnetization was recorded. The cooling and heating rate was kept constant at 2 K min^{-1} during the entire measurement period. The recorded magnetization profile has been shown in Fig. 10 which suggests that the heating curve exhibits wiggles at all the points where the field was switched off and on during cooling cycle. The memory experiment has revealed that the sample can remember the temporal and spatial variation of magnetic field and successfully recollect its past history on recovering the same temperature. This type of memory effect is emblematic manifestation of the fact that the sample exhibits spin glass like slow dynamics at low temperature.^{9,56–59} The presence of collective magnetic state along with frustrated magnetic interaction at the surface region are the underlying reason for having slow dynamics and memory behavior in the sample. It may be noted that for samples exhibiting collective magnetic excitation no unique ground state of anisotropy energy exists but rather the anisotropy energy of the system shows multiple minima in phase space. For such configuration of anisotropy energy, the system can approach toward equilibrium but cannot be able to reach it and this leads to spin glass like slow dynamics in the system.⁶⁰ By tagging the “H drop” as

0 and “H rise” as 1 we can easily store binary number in the sample and same can be recovered back by warming the sample in a constant magnetic field. Thus the sample can be used for sensing the spatial and temporal variation of magnetic field and coding, storing and retrieving of binary number through magnetic field change.

Catalysis

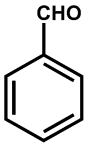
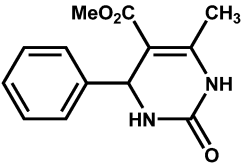
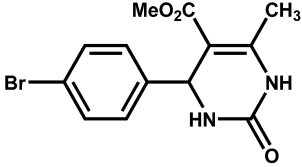
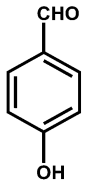
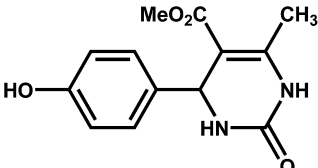
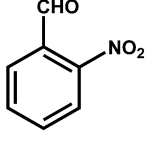
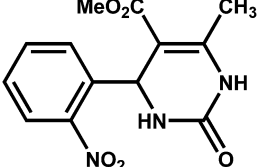
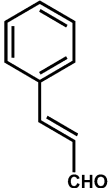
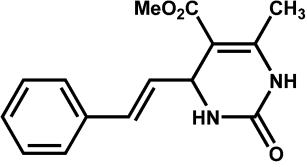
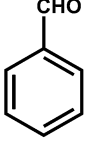
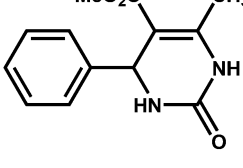
The high surface acidity and BET surface area together with the magnetic separation potential of the sample have motivated us to explore its activity as heterogeneous catalyst for the synthesis of 3,4-dihydropyridin-2-1*H*-(ones) (DHPM) *via* solvent-free one-pot Biginelli condensation reaction. We have carried out the

reactions with a wide range of substituted aldehydes, methyl acetoacetate and urea. The products were characterized by ^1H and ^{13}C NMR.⁶⁴ The results are listed in Table 4. The yield of the DHPM products as calculated from the weight ranged *ca.*, 60–75% for different aldehydes. When the reaction was carried out in the absence of any catalyst under similar reaction conditions no desired product was obtained. This result suggests that this mechanically activated nanosized Ni/Zn-ferrite is highly reactive catalyst for this acid catalytic condensation reaction.³²

Reusability of the catalyst

After separating the used catalyst magnetically, it was washed several times with ethyl acetate and dried in the oven. Further,

Table 4 Biginelli condensation reactions over nanosized Ni/Zn-ferrite catalyst

Entry	Aldehyde	Products	Time (min)	Yield (%)	TOF ^a (h ⁻¹)
1			10	67	708
2			10	73	771
3			10	71	749
4			10	65	687
5			10	66	696
6			10	No product	—

^a TOF = mol converted/mol of active site/time. Total acidity 1.516 mmol g⁻¹ (obtained from TPD-NH₃ analysis).

we have reused this catalyst for four consecutive cycles and it was found that the catalyst was reusable without any significant loss of activity. For entry 1 of Table 4, the yield decreased from 67% to 64% after fourth cycle and in other cases yield did not change significantly. Compared to filtration and centrifugation, the magnetic separation is a simpler and easier procedure for recovering the catalyst from the reaction mixture with minimum loss of the catalyst. Thus this magnetically separable nanosized Ni/Zn-ferrite material has large potential to be used as heterogeneous catalyst compared to other related non-magnetic catalysts reported in the literature.

Conclusion

The mechano-synthesized nanometric (~ 12 nm) $\text{Ni}_{0.45}\text{Zn}_{0.55}\text{Fe}_2\text{O}_4$ possesses good crystalline character and nearly equilibrium cation distribution $((\text{Fe}^{3+}_{0.45}\text{Zn}^{2+}_{0.55})_A[\text{Fe}^{3+}_{1.55}\text{Ni}^{2+}_{0.45}]_B\text{O}_4)$ and it exhibits stable magnetic order, good amount of coercive field (280 Oe) and high saturation magnetization (~ 53 emu g^{-1}) at room temperature. We have shown that the high energy ball milling induced enhancement of stress and surface anisotropy helps in retaining stable magnetic order of ferrite nanoparticles at room temperature and the reduction of magnetization due to spin canting can be counteracted by tuning the cation distribution in the sample in a favorable manner. These intriguing magnetic characters of the sample can be successfully used for the fabrication of magnetic data storage and recording devices by overcoming the impediments of miniaturization. Furthermore, the sample is able to store the memory of sudden changes in magnetic field while cooling and it can reminisce the changes during heating that can be used in coding, storing and retrieving of binary number through magnetic field change. It can also be used to detect the spatial and temporal variation of magnetic field. Further, the sample is highly porous and it contains both micropores (0.94 nm) and mesopores (6.4 nm). High catalytic efficiency together with easily recovery of the magnetic $\text{Ni}_{0.45}\text{Zn}_{0.55}\text{Fe}_2\text{O}_4$ nanocatalyst for the synthesis of one pot synthesis of 3,4-dihydropyrimidine-2(1H)-ones (DHPMs) suggested its further utility as a heterogeneous catalyst in future.

Acknowledgements

One of the authors (SD) gratefully acknowledges the financial support of Jadavpur University for providing research fellowship. RG acknowledges CSIR, New Delhi for a senior research fellowship. The UPE program of UGC and the PURSE program of DST, Govt. of India are also acknowledged. We are thankful to UGC-DAE CSR, Indore Center for infield Mössbauer measurement. We also gratefully acknowledge Prof. R. N. Joarder (Retd.) for helpful discussion.

Notes and references

- J. L. Dormann and M. Nogues, *J. Phys.: Condens. Matter*, 1990, **2**, 1223.
- R. H. Kodama, A. E. Berkowitz, E. J. McNiff and S. Foner, *Phys. Rev. Lett.*, 1996, **77**, 394.
- B. Ghosh, S. Kumar, A. Poddar, C. Mazumdar, S. Banerjee, V. R. Reddy and A. Gupta, *J. Appl. Phys.*, 2010, **108**, 034307.
- B. H. Liu, J. Ding, Z. L. Dong, C. B. Boothroyd, J. H. Yin and J. B. Yi, *Phys. Rev. B: Condens. Matter Mater. Phys.*, 2006, **74**, 184427.
- V. Šepelák, A. Feldhoff, P. Heitjans, F. Krumeich, D. Menzel, F. J. Litterst, I. Bergmann and K. D. Becker, *Chem. Mater.*, 2006, **18**, 3057.
- C. Cannas, A. Ardu, A. Musinu, D. Peddis and G. Piccaluga, *Chem. Mater.*, 2008, **20**, 6364.
- C. Pereira, A. M. Pereira, X. Fernandes, M. Rocha, R. Mendes, M. P. Fernández-García, A. Guedes, P. V. Tavares, J. M. Grenèche, J. P. Araújo and C. Freire, *Chem. Mater.*, 2014, **24**, 1496.
- B. K. Chatterjee, K. Bhattacharjee, A. Dey, C. K. Ghosh and K. K. Chattopadhyay, *Dalton Trans.*, 2014, **43**, 7930.
- S. Dey, S. K. Dey, K. Bagani, S. Majumder, A. Roychowdhury, S. Banerjee, V. R. Reddy and S. Kumar, *Appl. Phys. Lett.*, 2014, **105**, 063110.
- A. Goldman, *Modern Ferrite Technology*, Van Nostrand, Reinhold, New York, 1990.
- K. Vamvakidis, M. Katsikini, D. Sakellari, E. C. Paloura, O. Kalogirou and C. Dendrinou-Samara, *Dalton Trans.*, 2014, **43**, 12754.
- S. K. Gore, R. S. Mane, M. Naushad, S. S. Jadhav, M. K. Zate, Z. A. Allothman and B. K. N. Hui, *Dalton Trans.*, 2015, **44**, 6384.
- M. Menelaou, K. Georgoula, K. Simeonidis and C. Dendrinou-Samara, *Dalton Trans.*, 2014, **43**, 3626.
- P. Das, A. Dutta, A. Bhaumik and C. Mukhopadhyay, *Green Chem.*, 2014, **16**, 1426.
- H. J. Cui, J. W. Shi, B. Yuan and M. L. Fu, *J. Mater. Chem. A*, 2013, **1**, 5902.
- S. Dey, S. K. Dey, B. Ghosh, V. R. Reddy and S. Kumar, *Mater. Chem. Phys.*, 2013, **138**, 833.
- N. Ponpandian, A. Narayanasamy, C. N. Chinnasamy, N. Sivakumar, J. M. Grenèche, K. Chattopadhyay, K. Shinoda, B. Jeyadevan and K. Tohji, *Appl. Phys. Lett.*, 2005, **86**, 192510.
- M. Jalaly, M. H. Enayati, P. Kameli and F. Karimzadeh, *Physica B: Condensed Matter*, 2010, **405**, 507.
- S. Verma, P. A. Joy and S. Kurian, *J. Alloys Compd.*, 2011, **509**, 8999.
- N. Sivakumar, A. Narayanasamy, N. Ponpandian, J. M. Grenèche, K. Shinoda, B. Jeyadevan and K. Tohji, *J. Phys. D: Appl. Phys.*, 2006, **39**, 4688.
- S. Dey, S. K. Dey, B. Ghosh, P. Dasgupta, A. Poddar, V. R. Reddy and S. Kumar, *J. Appl. Phys.*, 2013, **114**, 093901.
- M. Kooti and M. Afshari, *Sci. Iran.*, 2012, **19**(6), 1991.
- Q. Wan, P. Li, J. Shan, F. Zhai, Z. Li and X. Qu, *J. Phys. Chem. C*, 2015, **119**, 2925.
- T. Liu, L. Wang, P. Yang and B. Hu, *Mater. Lett.*, 2008, **62**, 4056.
- K. Yan, X. Wu, X. An and X. Xie, *J. Alloys Compd.*, 2013, **552**, 405.

- 26 N. Velinov, K. Koleva, T. Tsoncheva, E. Manova, D. Paneva, K. Tenchev, B. Kunev and I. Mitov, *Catal. Commun.*, 2013, **32**, 41.
- 27 C. Singh, A. Goyal and S. Singhal, *Nanoscale*, 2014, **6**, 7959.
- 28 Y. L. N. Murthy, B. S. Diwakar, B. Govindh, K. Nagalakshmi, I. V. K. Viswanath and R. Singh, *J. Chem. Sci.*, 2012, **124**, 639.
- 29 A. M. Kulkarni, U. V. Desai, K. S. Pandit, M. A. Kulkarni and P. P. Wadgaonkar, *RSC Adv.*, 2014, **4**, 36702.
- 30 C. O. Kappe, *Acc. Chem. Res.*, 2000, **33**, 879.
- 31 J. Azizian, A. A. Mohammadi, A. R. Karimi and M. R. Mohammadzadeh, *Appl. Catal., A*, 2006, **300**, 85.
- 32 M. Pramanik and A. Bhaumik, *ACS Appl. Mater. Interfaces*, 2014, **6**, 933.
- 33 J. Mondal, T. Sen and A. Bhaumik, *Dalton Trans.*, 2012, **41**, 6173.
- 34 K. Lagarec and D. G. Rancourt, *Recoil-Mössbauer Spectral Analysis Software for Window*, University of Ottawa Press, Ottawa, 1998.
- 35 T. A. Anhøj, B. Bilenberg, B. Thomsen, C. D. Damsgaard, H. K. Rasmussen, C. S. Jacobsen, J. Mygind and S. Mørup, *J. Magn. Magn. Mater.*, 2003, **260**, 115.
- 36 A. Altomare, C. Giacovazzo, A. Guagliardi, A. G. G. Moliterni, R. Rizzi and E. J. Werner, *J. Appl. Crystallogr.*, 2000, **33**, 1180.
- 37 P. E. Werner, L. Eriksson and M. J. Westdahl, *J. Appl. Crystallogr.*, 1985, **18**, 367.
- 38 A. Boultif and D. Louer, *J. Appl. Crystallogr.*, 2004, **37**, 724.
- 39 A. Altomare, R. Caliandro, M. Camalli, C. Cuocci, C. Giacovazzo, A. G. G. Moliterni and R. Rizzi, *J. Appl. Crystallogr.*, 2004, **37**, 1025.
- 40 L. Lutterotti, *MAUDWEB, Version 1.9992*, 2004.
- 41 S. Dey, S. K. Dey, S. Majumder, A. Poddar, P. Dasgupta, S. Banerjee and S. Kumar, *Physica B: Condensed Matter*, 2014, **448**, 247.
- 42 S. Majumder, S. Dey, K. Bagani, S. K. Dey, S. Banerjee and S. Kumar, *Dalton Trans.*, 2015, **44**, 7190.
- 43 A. C. Larson and R. B. von Dreele, General structure analysis system (GSAS), *Report LAUR*, Los Alamos National Laboratory, 2000, pp. 86–748.
- 44 B. H. Toby, *J. Appl. Crystallogr.*, 2001, **34**, 210.
- 45 Y. Köseoğlu, A. Baykal, F. Gözüak and H. Kavas, *Polyhedron*, 2009, **28**, 2887.
- 46 S. Dutta, S. De, A. K. Patra, M. Sasidharan, A. Bhaumik and B. Saha, *Appl. Catal., A*, 2011, **409–410**, 133.
- 47 R. N. Bhowmik, R. Ranganathan, R. Nagarajan, B. Ghosh and S. Kumar, *Phys. Rev. B: Condens. Matter Mater. Phys.*, 2005, **72**, 094405.
- 48 R. N. Bhowmik, R. Ranganathan, S. Sarkar, C. Bansal and R. Nagarajan, *Phys. Rev. B: Condens. Matter Mater. Phys.*, 2003, **68**, 134433.
- 49 C. N. Chinnasamy, A. Narayanasamy, N. Ponpandian, K. Chattopadhyay, H. Guertal and J. M. Grenèche, *J. Phys.: Condens. Matter*, 2000, **12**, 7795.
- 50 B. Ghosh and S. Kumar, *Hyperfine Interact.*, 2008, **183**, 163.
- 51 S. Bid, A. Banerjee, S. Kumar, S. K. Pradhan, U. De and D. Banerjee, *J. Alloys Compd.*, 2001, **326**, 292.
- 52 G. F. Goya, T. S. Berquó, F. C. Fonseca and M. P. Morales, *J. Appl. Phys.*, 2003, **94**, 3520.
- 53 C. R. Alves, R. Aquino, J. Depeyrot, T. A. P. Cotta, M. H. Sousa, F. A. Tourinho, H. R. Rechenberg and G. F. Goya, *J. Appl. Phys.*, 2006, **99**, 08M905.
- 54 C. Cannas, A. Musinu, G. Piccaluga, D. Fiorani, D. Peddis, H. K. Rasmussen and S. Mørup, *J. Chem. Phys.*, 2006, **125**, 164714.
- 55 K. He, C. Y. Xu, L. Zhen and W. Z. Shao, *Mater. Lett.*, 2008, **62**, 739.
- 56 S. Chakraverty, B. Ghosh, S. Kumar and A. Frydman, *Appl. Phys. Lett.*, 2006, **88**, 042501.
- 57 Y. Sun, M. B. Salamon, K. Garnier and R. S. Averback, *Phys. Rev. Lett.*, 2003, **91**, 167206.
- 58 M. Sasaki, P. E. Jönsson, H. Takayama and H. Mamiya, *Phys. Rev. B: Condens. Matter Mater. Phys.*, 2005, **71**, 104405.
- 59 S. Chakraverty, M. Bandyopadhyay, S. Chatterjee, S. Dattagupta, A. Frydman, S. Sengupta and P. A. Sreeram, *Phys. Rev. B: Condens. Matter Mater. Phys.*, 2005, **71**, 054401.
- 60 M. Bandyopadhyay and S. Dattagupta, *Phys. Rev. B: Condens. Matter Mater. Phys.*, 2006, **74**, 214410.
- 61 ^1H and ^{13}C NMR data of some of the condensation products reported in Table 4. 5-Methoxycarbonyl-4-phenyl-6-methyl-3,4-dihydropyridin-2(1H)-one (entry 1). ^1H NMR (DMSO- d_6 , 500 MHz): δ (ppm): 9.17 (s, 1H), 7.71 (s, 1H), 7.18–7.30 (m, 5H), 5.10 (d, $J = 3$ Hz, 1H), 3.50 (s, 3H), 2.22 (s, 3H); ^{13}C NMR (DMSO- d_6 , 125 MHz): δ (ppm): 166.4, 152.7, 149.2, 145.3, 129.0, 127.8, 126.7, 99.6, 54.4, 51.3, 18.4. 5-Methoxycarbonyl-4-(4-bromophenyl)-6-methyl-3,4-dihydropyridin-2(1H)-one (entry 2). ^1H NMR (DMSO- d_6 , 500 MHz): δ (ppm): 9.26 (s, 1H), 7.78 (s, 1H), 7.51 (d, $J = 8.5$ Hz, 2H), 7.17 (d, $J = 8.5$ Hz, 2H), 5.12 (d, $J = 2.5$ Hz, 1H), 3.52 (s, 3H), 2.24 (s, 3H); ^{13}C NMR (DMSO- d_6 , 125 MHz): δ (ppm): 166.3, 152.5, 149.5, 144.6, 131.9, 129.0, 120.9, 99.1, 53.9, 51.4, 18.4. 5-Methoxycarbonyl-4-(4-hydroxyphenyl)-6-methyl-3,4-dihydropyridin-2(1H)-one (entry 3). ^1H NMR (DMSO- d_6 , 500 MHz): δ (ppm): 9.31 (s, 1H), 9.10 (s, 1H), 7.60 (s, 1H), 7.01 (d, $J = 8$ Hz, 2H), 6.67 (d, $J = 8.5$ Hz, 2H), 5.02 (s, 1H), 3.51 (s, 3H), 2.21 (s, 3H); ^{13}C NMR (DMSO- d_6 , 125 MHz): δ (ppm): 166.4, 157.0, 152.7, 148.5, 135.7, 127.8, 115.5, 99.9, 53.7, 51.2, 18.3. 5-Methoxycarbonyl-4-(2-nitrophenyl)-6-methyl-3,4-dihydropyridin-2(1H)-one (entry 4). ^1H NMR (DMSO- d_6 , 500 MHz): δ (ppm): 9.36 (s, 1H), 8.12–8.10 (m, 2H), 7.90 (s, 1H), 7.65–7.60 (m, 2H), 5.28 (d, $J = 3$ Hz, 1H), 3.52 (s, 3H), 2.26 (s, 3H). 5-Methoxycarbonyl-6-methyl-4-styryl-3,4-dihydropyrimidin-2(1H)-one (entry 5). ^1H NMR (DMSO- d_6 , 500 MHz): δ (ppm): 9.15 (s, 1H), 7.54 (1H, s), 7.23–7.40 (m, 5H), 6.36 (d, $J = 15$ Hz, 1H), 6.21 (dd, $J = 6$ Hz, 16 Hz, 1H), 4.72 (d, $J = 3$ Hz, 1H), 3.61 (s, 3H), 2.18 (s, 3H); ^{13}C NMR (DMSO- d_6 , 125 MHz): δ (ppm): 165.6, 152.6, 148.6, 136.2, 130.0, 128.6, 127.9, 127.5, 126.3, 97.6, 51.7, 50.8, 17.7, 14.2.